48. Friction and Wear in Micro- and Nanomachines

Maarten P. de Boer, Alex D. Corwin, Frank W. DelRio, W. Robert Ashurst

The prediction and characterization of multi-length-scale tribological phenomena is challenging, yet essential for the advancement of micro- and nanomachine technology. Here, we consider theoretical underpinnings of multiasperity friction, review various approaches to measure micro- and nanoscale friction, and discuss the effect of monolayer coatings to reduce friction. We then focus on test results from a friction-based actuator called a nanotractor. The experimental procedures and data analysis used to measure friction, adhesion force, and wear are detailed. We observe and discuss a variety of phenomena including nanoscale slip with an associated bifurcation in the transition to motion, contact aging and deaging, a stick–slip/steady sliding bifurcation behavior, and wear. We anticipate great progress towards reliable, contacting micro- and nanomachines by linking theory and experiment to nano- and microscale tribological phenomena and by improving the testing, materials, and processing methods used to characterize these phenomena.

Friction and wear phenomena present challenges and opportunities for micro- and nanosystems. In many possible applications, counterfaces rub against each other. Examples of how this can occur are illustrated in Fig. 48.1, where a close-up of features in a complex locking mechanism [48.1] are shown. Here, a large gear ratio is employed to amplify torque. The gear teeth mesh and rotate about hubs that are made by a five-structural-level polycrystalline silicon (polysilicon) surface micromachining technology at Sandia National Laboratories, known as the SUMMiT V process [48.2]. The gears are equipped with features known as dimples to minimize contact and hence adhesion with the substrate. The dimples also prevent the gears from tilting excessively, as does the guide shown at the top right of Fig. 48.1. The output gear meshes with a linear rack that is guided via long rails, and rubbing contact is also made there. To move from right to left, a pin must

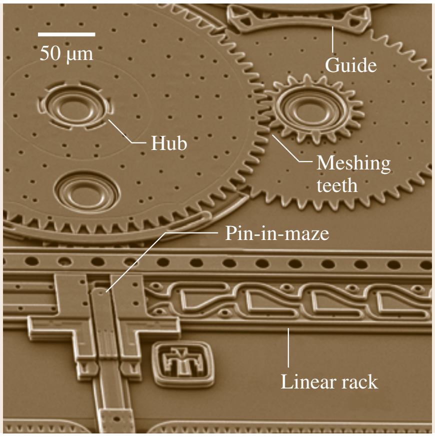

Fig. 48.1 Rubbing surfaces occur in many micromachine applications, and pose a reliability challenge. This figure shows an example of complex mechanical logic

correctly traverse a maze inside the linear rack. If an incorrect decision is made, a ratchet and pawl mechanism (not shown), which also requires rubbing contact, prevents resetting.

In the example shown in Fig. 48.1, friction is generally a parasitic effect and efforts are directed towards minimizing it. Eliminating friction in micromachines has proven difficult, yet therein lies opportunity. A number of researchers have chosen to take advantage of friction, achieving impressive micro- and nanoscale actuation performance. The actuators are microscale stepper motors with step sizes on the order of 10–100 nm, and with long travel ranges up to hundreds of μm. Also, their actuation forces can reach the mN scale. These characteristics compare favorably with the more commonly used comb drives, which typically move 10–20 μm and deliver forces in the low μN range. Such features make such stepper motors attractive, including for positioning for optical [48.5], data storage [48.6, 7], and medical [48.8] applications. We also envision that they may be very useful for testing properties of micro- and nanoscale specimens as well as for manipulating nanoscale instruments.

Several representative implementations of microscale linear actuators, in which actuation is based on frictional effects, are illustrated in Fig. 48.2. Each of these devices has unique design features, performance tradeoffs, and processing requirements. An asymmetric bushing geometry enables the motion of the scratch drive actuator (SDA) in Fig. 48.2a [48.3]. The layout and the drive signal for the SDA are simple, the device area is small ($\approx 30\,\mu m \times 100\,\mu m$), the applied voltage is moderate (30–100 V, depending on layer thicknesses), it travels unidirectionally a distance of 500 μm or more [48.9], and it generates reasonably large forces (tens of μN) [48.3]. A model that predicts operating voltages has been developed, but it does not treat frictional forces [48.10]. The shuffle motor [48.11] and nanotractor [48.12] ($150\,\mu m \times 600\,\mu m$) designs place voltage-controlled clamps at the ends of an actuator plate, enabling bidirectional motion. These actuators can be modeled well and the nanotractor, pictured in Fig. 48.2b, achieves a theoretical maximum force value of $F_{max} = 0.5$ mN [48.12]. A subsequent design known as the μWalker with two degrees of freedom has been demonstrated [48.4, 13] as shown in Fig. 48.2c. Both the nanotractor and the two-dimensional (2-D) μWalker achieve other theoretical expectations including step size on the order of tens of nm and velocity proportional to step frequency up to the mm/s range. The 2-D μWalker is realized in a four-mask process with two layers of structural polysilicon. It takes advantage of a Si_3N_4 coating for in-plane isolation of voltage applied to the clamps, and also as a mechanical layer to enhance wear characteristics. The nanotractor is fabricated in the SUMMiT V process and is also a model friction test structure.

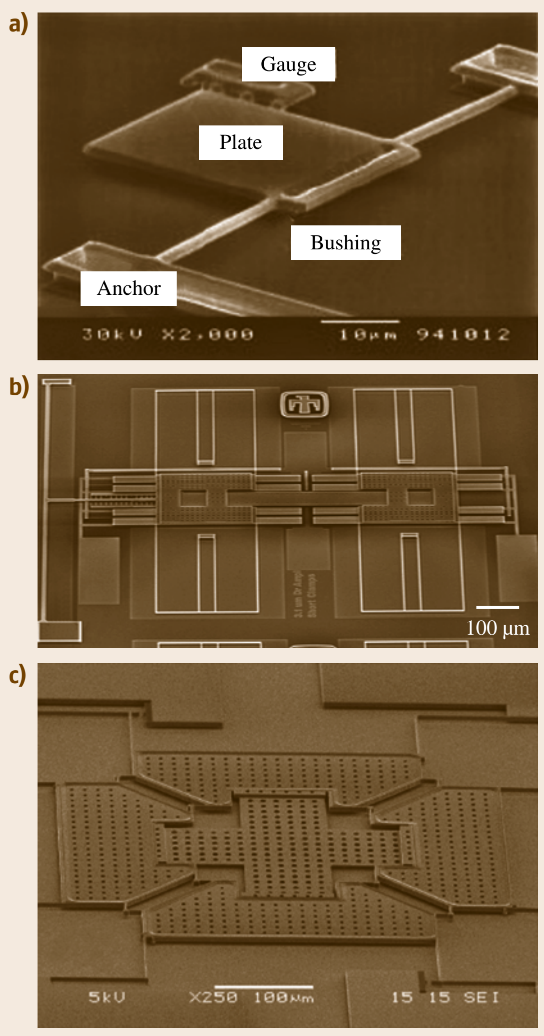

Fig. 48.2a–c Rubbing surfaces can also be used to create powerful actuators such as **(a)** scratch drive actuator (after [48.3], © IEEE by permission). **(b)** Nanotractor. **(c)** 2-D μWalker (after [48.4], © Koninklijke Bibliotheek, Den Haag)

In the following sections, we shall describe theoretical underpinnings of multiasperity friction, micromachined test structures to measure friction, and monolayer coatings that have been used to reduce friction in microelectromechanical systems (MEMS). The major focus of this chapter will then be on testing, metrology, friction, and wear in experiments with nanotractors.

48.1 From Single- to Multiple-Asperity Friction

According to *Amontons*' empirically deduced law [48.14], the friction force F_f is directly proportional to the applied normal load F_n and independent of the apparent contact area A_a as described by

$$F_\mathrm{f} = \mu F_\mathrm{n} \,, \tag{48.1}$$

where μ is the coefficient of friction. For surfaces at rest, the coefficient of static friction is denoted by μ_s, while for surfaces in relative motion, the coefficient of dynamic friction is denoted by μ_d.

By considering two surfaces in mechanical contact, it becomes clear that real surfaces are rough on the microscale, consisting of many peaks and valleys. Thus, the *real* contact area A_r between two surfaces is actually defined by the highest peaks, also known as asperities, and is much less than the *apparent* contact area A_a. *Bowden* and *Tabor* [48.15] presented the idea that friction is related to the real (as opposed to apparent) area of contact via two basic mechanisms: shearing and plowing. Shearing refers to the force required to break the junctions at contacting asperities, while plowing represents the force needed for a hard asperity to displace softer material. In the absence of plowing (i. e., for two materials with roughly the same hardness, as is usually the case in micromachined materials), friction is directly proportional to the real contact area via

$$F_\mathrm{f} = \tau A_\mathrm{r} \,, \tag{48.2}$$

where τ is the shear strength of the contact. Hence Amontons' law is recovered if A_r is proportional to normal load.

The proportionality between real contact area and applied load, however, seems to disappear for two asperities in *elastic* contact. *Hertz* [48.16] provided the first analysis of the stress distribution and displacement at the interface of two elastic spheres, which can be simplified to a sphere in contact with a flat. The total load F_n compressing a sphere of radius R into a flat surface can be related to the contact area A_r by

$$A_\mathrm{r} = \pi \left(\frac{3F_\mathrm{n}R}{4E^*} \right)^{\frac{2}{3}} \,, \tag{48.3}$$

where the combined elastic modulus of the two contacting surfaces $E^* = [(1-\nu_1^2)/E_1 + (1-\nu_2^2)/E_2]^{-1}$. *Johnson*, *Kendall*, and *Roberts* (JKR) later observed that the contact area between two rubber spheres was larger than that predicted by the Hertz theory and developed a model to account for the surface forces at the interface [48.17]. The model was based on a balance between the stored elastic energy, the mechanical energy in the applied load, and the surface energy. *Derjaguin*, *Muller*, and *Toporov* (DMT) used a thermodynamic approach to consider the molecular forces in and around the contact zone [48.18]. Unlike the JKR approach, though, the profile of the sphere outside of the contact area was assumed to be Hertzian (i. e., the surface forces are small enough that their effect on the deformation of the sphere can be neglected). Initially, the models seemed to contradict each other. *Tabor* [48.19] determined that the models represent the extreme ends of a spectrum, and developed a parameter μ_T to span the spectrum. Accordingly, the JKR theory is suitable

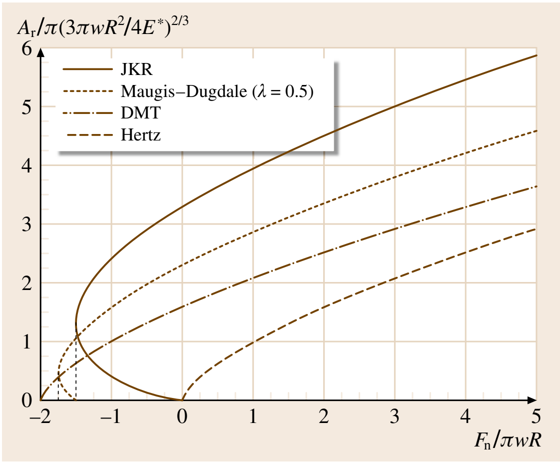

Fig. 48.3 Normalized A_r–F_n curves for the Hertz, DMT, Maugis–Dugdale, and JKR contact models. As the transition parameters μ_T and λ increase from zero to infinity, there is a continuous transition from the DMT to the JKR regime. In the absence of adhesion, all of the models approach the Hertzian case. The work of adhesion is w

for elastically compliant materials with a large radius and surface energy, while the DMT theory is appropriate for elastically stiff materials with a small radius and surface energy. *Maugis* [48.20] later developed a semi-analytical solution using a Dugdale approximation; the transition from DMT to JKR was described in terms of the parameter λ, which is related to μ_T via $\lambda = 1.16\mu_T$. Figure 48.3 illustrates the relationship between A_r and F_n for all of these models. In the presence of attractive forces, the contact area increases at a given load, which increases the friction force, as depicted by (48.2). More importantly, all of the models exhibit a nonlinear relationship between real contact area and applied load, contradicting expectations from Amontons' law.

A number of researchers [48.22–24] have successfully used the aforementioned single-asperity relationships to model friction measurements taken via friction force microscopy (FFM). However, micro- and nanodevices fabricated using surface micromachining techniques often have contacting surfaces with nanometer-scale surface roughness. As a result, it becomes important to develop *multiple*-asperity contact models to elucidate the impact of surface topography on the relationship between contact area and applied load. In the simplest case, the rough surface consists of a series of asperities all at the same height, as shown in Fig. 48.4a. Here, the applied load is divided evenly among all of the contacting asperities, which results in $A_r \propto F_n^{2/3}$. *Archard* [48.21, 25] improved on this idea by considering a *uniform* distribution of spherical asperities (radii of curvature R_1) in contact with a rigid flat as shown in Fig. 48.4b. For elastic deformation, $A_r \propto F_n^{4/5}$. To examine multiscale roughness, a second set of protuberances (radii of curvature R_2) can be evenly distributed over the surface of the existing spheres, such that $R_2 \ll R_1$, as shown in Fig. 48.4c. In this case, $A_r \propto F_n^{14/15}$. With even smaller protuberances of radius R_3, as shown in Fig. 48.4d, the relationship becomes $A_r \propto F_n^{44/45}$. This indicates that proportionality between area and load is not necessarily the result of plastic flow in the contact zones, as originally proposed, but can be due to elastic contact between rough surfaces.

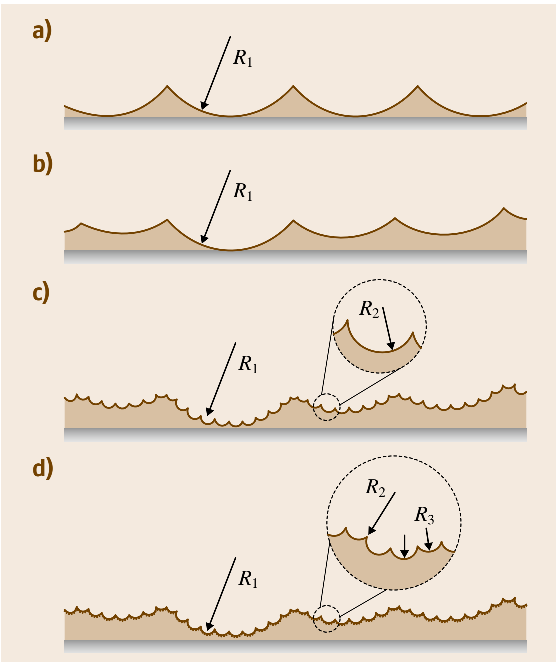

Fig. 48.4a–d Multiple-asperity models from [48.21]. Assuming elastic deformation, the relationship between the contact area A_r and the applied load F_n are **(a)** $A_r \propto F_n^{2/3}$, **(b)** $A_r \propto F_n^{4/5}$, **(c)** $A_r \propto F_n^{14/15}$, and **(d)** $A_r \propto F_n^{44/45}$. In general, the index n in the relationship $A_r \propto F_n^n$ ranges from $\frac{2}{3}$ for a series of asperities at the same height to ≈ 1 for a multiple-asperity surface with several sets of protuberances

Greenwood and *Williamson* (GW) considered a *statistical* distribution of N asperities with constant radius of curvature R in contact with a flat surface [48.26]. For a Gaussian distribution of asperity heights, A_r is almost exactly proportional to F_n. *Fuller* and *Tabor* [48.27] extended the GW model for JKR contacts to study rough surface adhesion and defined the adhesion parameter θ, which represents the competition between the compressive forces exerted by the higher asperities and the adhesive forces acting between the lower asperities (analogous to the Tabor parameter). In a similar manner, *Maugis* [48.28] extended the GW model for DMT contacts. For infinite θ (work of adhesion $w = 0$), the Maugis theory is equivalent to the GW model and $A_r \propto F_n$. On the other hand, as θ decreases (w increases), the relationship between contact area and applied load becomes more nonlinear.

48.1.1 Micromachined Test Structures

From this survey of multiple asperity contact models, we see that (1) adhesive forces and (2) asperity distribution can significantly impact the relationships between friction force, contact area, and applied load. Therefore, although widely observed, Amontons' law is not necessarily expected. While there are techniques in place to convert topographic data from real surfaces into Gaussian asperity distribution data [48.29], it is unclear as to whether these statistical models accurately represent the surface topography [48.30]. Therefore, it becomes necessary to fabricate micromachined test structures that can measure friction directly. Moreover, micromachined structures are appropriate test vehicles for studying friction and wear because their performance will reflect any effects that are due to details of the fabrication process. These include technologically relevant issues such as the effect of sidewall slope on vertical surfaces, surface roughness, and the ability to coat micromachined structures with friction-reducing coatings in spite of sometimes tortuous access paths.

One of the earliest systematic studies of microscale friction was carried out by *Howe* and coworkers at UC Berkeley [48.33]. Since then, a number of researchers have investigated this critical issue using a variety of techniques and devices. A common approach is to design a moveable beam that can be brought into contact and slid against a counter surface (see, e.g., [48.31, 34–39]). An example from [48.31] is shown in Fig. 48.5a,b. The measurements from this study showed that statistical contact models as described above may not apply to lightly loaded, small apparent contact areas in MEMS. This is because such models would predict less than one contact within the contact area. The researchers also found that adhesion between the surfaces must be recognized as an important contribution to the applied normal load. Most microdevice friction work has involved so-called *sidewall* devices such as this one, where the contacting surfaces are the result of an etching procedure and may have vertical striations and significant directional anisotropies. The topography of sidewalls is influenced by lithography, etching, *and* grain boundaries as seen in Fig. 48.5c [48.32], and often exhibits significantly higher roughness than in-plane surfaces where topography is primarily determined by grain growth and etching phenomena.

Komvopoulos and coworkers [48.38] developed a sidewall microscale friction device that involved a push drive and a shear drive. Testing of the device consisted of first loading the contact and then shearing the newly formed interface while monitoring the position of the shear drive with a charge-coupled device (CCD) camera, with a spatial resolution of about 0.3 µm. It was shown that the engineering coefficient of friction exhibited a nonlinear dependence on contact pressure that was unique to the testing environment; higher friction was observed at higher humidity levels. Further, the adhesion forces, significant at the microscale, added substantially to the friction when the external load was comparable to the adhesion force [48.38].

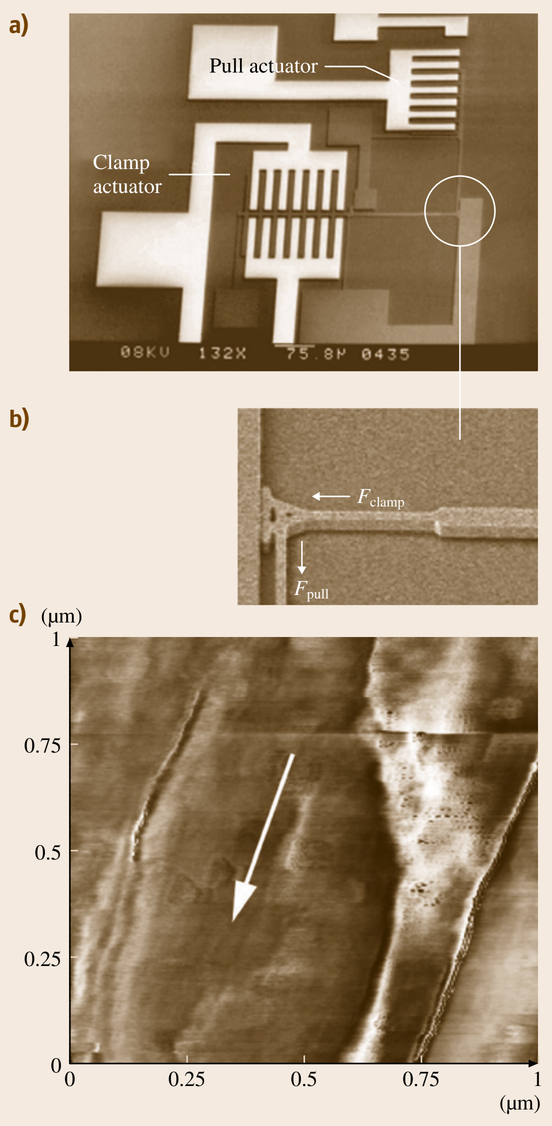

Fig. 48.5 **(a)** A MEMS test structure **(b)** designed to measure sidewall friction (after [48.31], © VSP). **(c)** Topographical image of a sidewall surface, where the root-mean-square (RMS) roughness is 40 nm (after [48.32], © Xavier by permission)

Frenken and coworkers recently developed a similar sidewall device, but included an on-device, real-time, electrical capacitance readout mechanism for high-resolution displacement measurement (about 4 nm peak-to-peak noise sensitivity). Their device, called the *Leiden MEMS tribometer*, consists of two orthogonally oriented comb drives that are used to position a test slider against a fixed surface. The comb drives are used to generate loading and shearing forces on the contact surface. They indicated two regimes in the friction behavior depending on the load. For the low-loading regime, a wearless stick–slip phenomenon is observed which is repeatable over many cycles but stochastic in position and presumably related to the details of the topography. In the high-loading regime, wear was observed, and although the stick–slip behavior exhibited in the low-load regime disappeared, the motion was not smooth, as ongoing wear processes altered the surface topography and changed the contact mechanics [48.37].

48.1.2 Monolayer Lubrication in Nano- and MEMS Tribology

While the results in the previous section are certainly interesting, the effects of monolayer coatings, which significantly reduce friction, were not studied. It has been well established that monolayer lubricants are effective at reducing friction at the nanoscale. Much of this knowledge has been achieved through nanotribology experiments involving atomic force microscopy (AFM) [48.40, 41] or a surface forces apparatus (SFA) [48.42] where ideal systems (i. e., pristine environments, single crystal substrates, perfect monolayers, etc.) are employed to probe fundamental aspects of friction phenomena using single-asperity contacts.

Nanotribology studies have shown significant (and sometimes conflicting) impact of monolayer thickness (i. e., precursor chain length) and terminal group on friction [48.43–46]. Similar to rough surfaces, there are two basic phenomena involved in single-asperity friction: plowing and shearing [48.41]. With regard to monolayer coatings, plowing refers to the action of the asperity tip deforming the monolayer, thereby dissipating energy by introducing chain defects that may elastically relax after the tip has passed, while shearing refers to the localized disruption of intermolecular forces as a result of the shear interaction of the film surface with the tip. Some researchers report an increase in friction as chain length increases [48.47], while others report a decrease in friction [48.45]. These conflicting findings suggest that additional experimental factors contribute to the frictional behavior of monolayer films, and the operating conditions must be considered in the friction study.

As discussed above, the friction force may be proportional to the true contact area, leading to a nonlinear dependence of friction with load. This has been supported by experimental data for inorganic materials. However, in many studies of organic monolayers, a linear relationship is found [48.43, 45, 48–50]. This could be attributed to plastic deformation, or to multiple contacting nanoasperities on the single AFM tip, or to viscoelastic deformation during the sliding. It is important to note that many of the fundamental mechanistic studies of nanoscale friction have involved high-modulus inorganic materials with similar bulk and surface properties. Since monolayers are comparatively compliant materials, usually deposited on a stiff material, the validity of applying findings from such fundamental studies to monolayer systems can be questioned. Another aspect to consider is that deviation from linearity as in the JKR model [48.17] may be small and experimentally obscured for low loadings, typical of AFM studies [48.41]. Recently, a continuum thin coating theory has been developed to address these issues [48.51, 52].

Some researchers have successfully applied monolayer films to micromachines for the purpose of studying their effects on friction [48.12, 53–56]. The most convenient monolayers to apply to polysilicon microdevices involve silane-based linking reactions with the oxide layer present on the surface. From the silane class of materials, the most commonly studied monolayer film is that produced by octadecyltrichlorosilane (OTS). This particular film has received much attention in the literature due to its self-assembly characteristics [48.57]. Recent work using AFM methods has shown that the friction behavior of the film is dependent on the local 2-D phase (liquid expanded or liquid condensed) at the asperity contact [48.58] and that liquid condensed phases are likely to be associated with grain-boundary areas for polysilicon devices [48.59]. OTS films have been utilized as antifriction layers for MEMS devices and studied in that capacity. It is generally accepted by the MEMS community that OTS and other monolayer films reduce the friction of microdevices when properly integrated and applied to the device.

Clearly, it would be interesting to link single-asperity measurements made by nanotribologists to multiasperity measurements made by MEMS tribologists. This would involve a detailed understanding of the surface properties, loading characteristics, and topography. Indeed, asperity radii of polycrystalline silicon are on the order of 20–200 nm, in the same range as AFM tips. However, the richness of MEMS tribology measurements, such as the nonlinear effect of pressure [48.38] and wearless regime [48.37] mentioned above, are only beginning to be explored. At the macroscale, friction measurements have revealed complex behavior including aging, velocity dependence, and stick–slip bifurcations, and a theory known as *rate-and-state* friction has been advanced [48.60–64]. This development comes from detailed measurements with different combinations of springs and different puller velocities, and it applies to a wide range of materials from rock [48.61] to cardboard [48.62] to plastic [48.65]. This theory applies the notion of contact rejuvenation and solves coupled differential equations of rate (instantaneous velocity) and state (contact age) variables [48.66, 67]. Quite possibly, microscale friction will have related dependencies. As an initial effort to explore some of these potential dependencies, the loading protocol has been varied in a systematic fashion using the nanotractor. As we shall see, strong effects that may be related to rate-and-state friction are observed.

48.2 Nanotractor Device Description

The findings assembled from uncoated and coated sidewall devices have significant value to the MEMS community and provide guidance on how to more reliably design and operate microdevices. However, statistical contact mechanics models, which rely on numerous contacts, do not apply because of the small contact areas and nonvertical nature of sidewall etching. On the other hand, the nanotractor achieves uniform loading over a large area of in-plane surfaces during friction testing so that such models will apply.

Figure 48.6a is a scanning electron microscopy (SEM) cross section showing the details of how the nominally flat model frictional interface is created in the clamp regions. Normal force is symmetrically applied via the electrodes to the right and left of the counterfaces. The counterfaces are each electrically grounded and make mechanical contact. The air gap breaks down at 300 V; the device is actuated at 200 V or less to avoid any issues with electrostatic damage. The inset shows that the upper counterface is nominally flat, meaning that calculations of real contact area from statistical theories [48.26, 29, 30, 68, 69] can be used without having to make a correction for surface tilt or curvature. This counterface is 3 µm wide, and there are two such counterfaces in each clamp. The length of the clamps in the results reported below is 600 µm. Hence the total apparent contact area for both friction clamps is

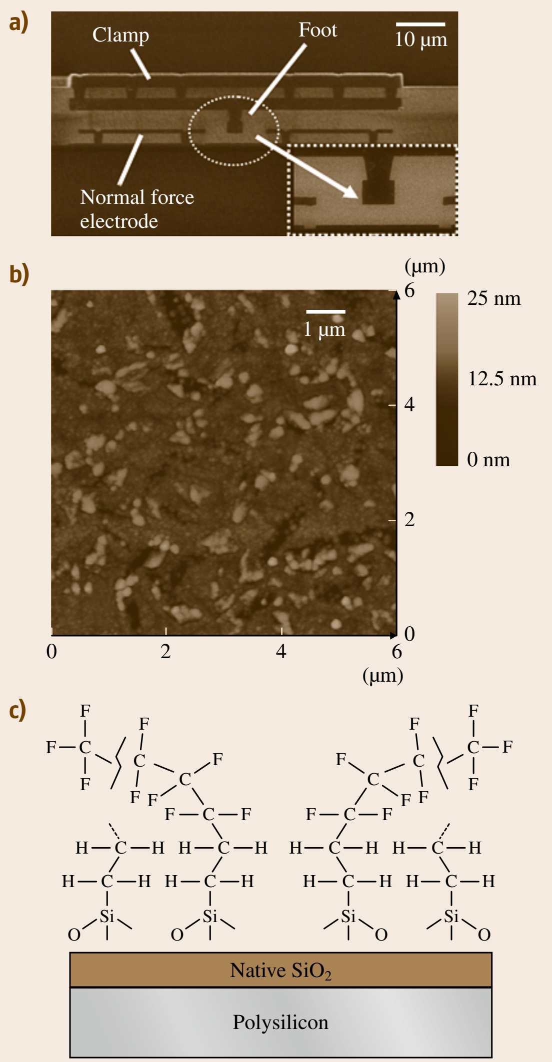

Fig. 48.6 (a) Nanotractor SEM cross section through a clamp. The *inset* shows the detail of the frictional counterfaces. The oxide material surrounding the polysilicon is removed by HF acid etching prior to monolayer lubricant deposition. **(b)** AFM micrograph of a typical polysilicon surface after coating with a FOTAS organic monolayer. **(c)** Schematic representation of the disordered FOTAS monolayer, with some chains bending out of the plane of the paper ▶

$A_a = 7200\,\mu m^2$. The electrode area enables continuous control of normal load F_n up to $\approx 10\,mN$, where F_n is proportional to V_c^2. Here, V_c is the clamping voltage.

Figure 48.6b shows the surface roughness, which is mainly due to the grain structure on these surfaces (i. e., not due to plasma etching), with a typical root-mean-square value of 5 nm. Although the contact geometry is much improved, it remains a challenging task to calculate the real contact area accurately. In one approach, *DelRio* et al. [48.70] imported data from AFM surface topography maps and conducted pixel-by-pixel analysis to show that adhesion in MEMS is dominated by van der Waals forces across noncontacting surfaces. Agreement within a factor of two with the experimental data was obtained. A voxel calculation based on directly imported data has also been used to better estimate the areas of real contact between polycrystalline gold MEMS surfaces [48.71]. It would also be of interest to apply a theory that incorporates skew and kurtosis [48.69], or a theory that calculates real contact area by solving a diffusion equation of an autocorrelated surface power spectrum [48.30].

The experimental data that follows were measured using nanotractors coated by a 1.2 nm-thick monolayer coating (tridecafluoro-1,1,2,2-tetrahydrooctyl-*tris* (dimethylamino)silane, $CF_3C_5F_{10}C_2H_4Si(N(CH_3)_2)_3$, FOTAS) deposited from the vapor phase [48.72]. This monolayer is represented schematically in Fig. 48.6c. The eight-carbon-chain molecule has a sufficiently high vapor pressure to allow vapor-phase deposition, which makes it highly reproducible in a manufacturing setting. However, it is too short to form a self-assembled monolayer; rather the chains attached to the surface are believed to be somewhat disordered. This lack of order may be responsible for the memory effects reported below.

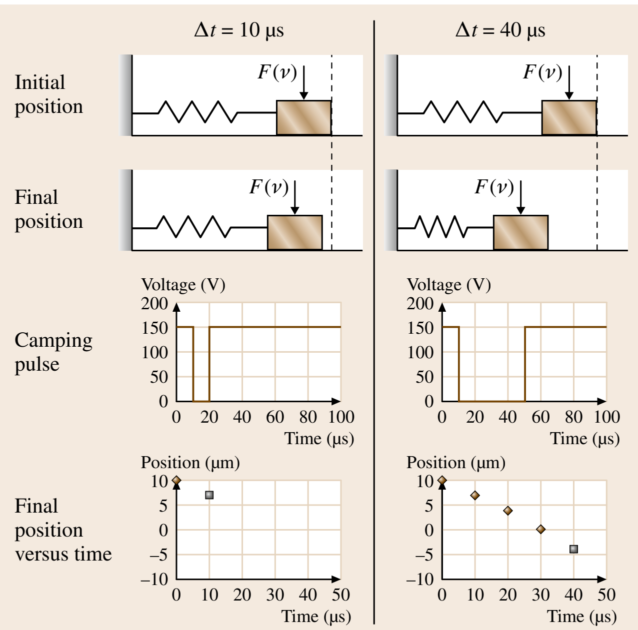

Fig. 48.7 Electromechanical strobing method to capture MEMS friction dynamics

48.2.1 Nanotractor Dynamic Friction Measurement

In studying its dynamic motion, the nanotractor can be simply thought of as a mass and a spring, riding atop a planar surface, with a normal force generated by electrostatics. By walking the nanotractor (as described in [48.12]), the mass can be pulled out to some distance, and then released. The resulting motion will be influenced by both air damping (dependent on the pressure) and Coulomb friction damping (depending on the normal force exerted on the mass), as well as adhesive force between the mass and the plane. For suitably small friction, the mass can be expected to oscillate several times about its zero position with decaying amplitude before finally coming to rest.

Corwin and *de Boer* have developed a mechanical stop motion technique for studying this motion [48.54] through the use of pulsed clamping, shown diagrammatically in Fig. 48.7. They walk the nanotractor out to a specified position ($x_0 = 10\,\mu m$ for the example shown). The position is determined using a high-accuracy, subpixel interpolated pattern-matching technique (from National Instruments Vision Toolkit as utilized in scripting software developed at Sandia National Laboratories called MEMScript). With a 50× objective, this technique achieves approximately 5 nm in-plane resolution. Once the nanotractor is walked to x_0 (within $\approx 50\,nm$ as limited by its step size), it is held in place solely by the electrostatic clamp between two polysilicon surfaces. The clamp is then released for $10\,\mu s$, and then clamped again (clamping time is about $1\,\mu s$). The position of the clamp is recorded using pattern matching, and the nanotractor is again walked back to the specified position. The clamp is now released for $20\,\mu s$ and its position is recorded. The same procedure is repeated for $30\,\mu s$, $40\,\mu s$, etc., continuing until the resting position of the nanotractor no longer changes with release duration. The position of the nanotractor

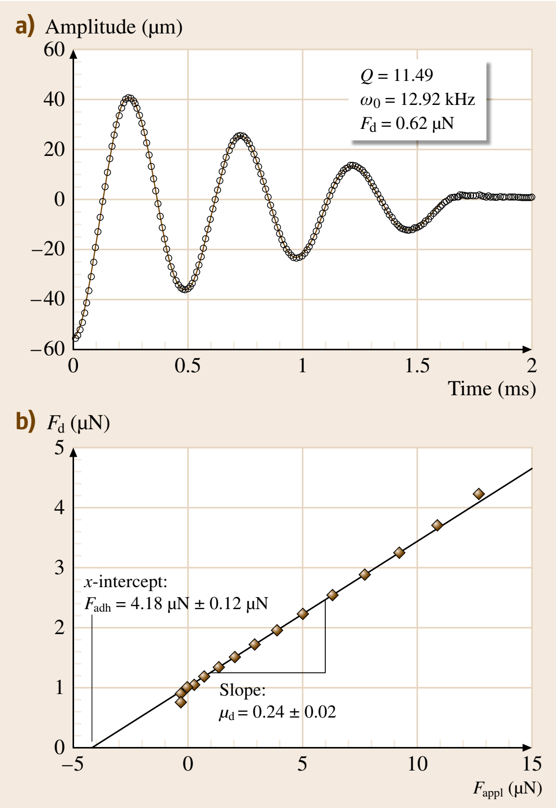

Fig. 48.8a,b Dynamic friction test results. **(a)** Position versus time data. **(b)** Friction force versus applied load data, which is used to find F_{adh} (after [48.54], © AIP by permission)

as a function of release duration can then be assembled into a position versus time plot, as is seen in Fig. 48.8 ($x_0 = -58\,\mu\mathrm{m}$ for these results).

The position data in Fig. 48.8 is modeled with a second-order nonlinear differential equation that takes into account both air damping and dry friction damping

$$m\ddot{x} + b\dot{x} + F_{\mathrm{d}}\mathrm{sgn}(\dot{x}) + kx = 0\,. \tag{48.4}$$

Here, the contribution from the air damping is written as a velocity-dependent force, $b\dot{x}$ (as the gap between the nanotractor and the substrate is small [48.73]), and the friction is written as $F_{\mathrm{d}}\mathrm{sgn}(\dot{x})$ where the sgn function simply returns 1 or -1 depending on the sign of the argument. Also, k is the spring constant of the folded beam suspension (shown schematically in Fig. 48.7) and m is the mass of the nanotractor.

Solving (48.4) piecewise analytically, the undamped resonant frequency ω_0, F_{d}, and the quality factor Q can be determined. The measured value of ω_0 is consistent with the expected resonant frequency given the nanotractor mass and the suspension spring constant. The experimentally determined quality factor, $Q = m\omega_0/b = 11.5$, is in good agreement with a first-order Couette calculation of $Q = 14.5$ [48.73]. The friction force F_{d} is nonzero even though the suspension spring provides a slight out-of-plane force (with spring constant k_z), indicating the presence of an adhesive force.

Following Amontons' law, the total frictional force is found by summing all normal forces as

$$F_{\mathrm{d}} = \mu_{\mathrm{d}}(F_{\mathrm{c}} + mg - k_z z) + \mu_{\mathrm{d}} F_{\mathrm{adh}}\,, \tag{48.5}$$

including the restoring force from the suspension spring ($k_z z$), the gravitational mass (mg), the electrostatic force on the clamp (F_{c}), and a surface attraction adhesive term (F_{adh}). Here the applied force is $F_{\mathrm{appl}} = F_{\mathrm{c}} + mg - k_z z$.

The value of μ_{d} is determined by repeating the procedure illustrated in Fig. 48.7, systematically increasing F_{c} and measuring the resulting F_{d}. The results are shown in Fig. 48.8b. Following (48.5), a line is fitted to extract both dynamic friction and adhesion. For the data shown, $\mu_{\mathrm{d}} = 0.24 \pm 0.02$ and $F_{\mathrm{adh}}/A_{\mathrm{a}} = 0.6\,\mathrm{nN}/\mu\mathrm{m}^2$. The latter value is somewhat smaller than the value of $6\,\mathrm{nN}/\mu\mathrm{m}^2$ extracted from adhesion models [48.70]. However, in this device the nanotractor foot was not entirely flat, an empirical difficulty that was corrected in later experiments.

With a nominally flat foot, *Corwin* and *de Boer* have recently demonstrated an improved version of this technique that minimizes the number of measurements required to determine the adhesion and dynamic friction of the nanotractor. The technique is detailed in [48.74], and reduces the problem to fitting linear curves over the first half-cycle of motion. The adhesion value found was $F_{\mathrm{adh}}/A_{\mathrm{a}} = 3\,\mathrm{nN}/\mu\mathrm{m}^2$, in reasonable agreement with the adhesion model calculation [48.70]. In subsequent measurements reported below, the foot is nominally flat, as shown in Fig. 48.6a.

48.2.2 Nanotractor Static Friction Measurements

To make a static friction measurement, the nanotractor is walked to an initial position and held in place with a prescribed normal force, as shown in Fig. 48.9a. The tangential force experienced during the hold is kx_0. The normal force F_{n} is then ramped down by lowering the clamp voltage. (Here it is assumed that $F_{\mathrm{n}} = F_{\mathrm{c}}$ because the other terms in (48.5) are small for large F_{n}).

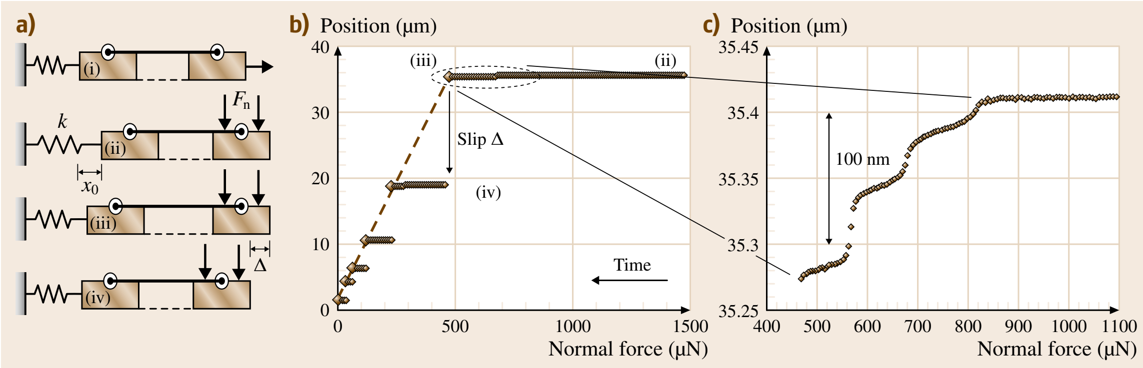

Fig. 48.9 **(a)** Schematic for the friction test. **(b)** Position versus normal force data at the micron scale. **(c)** Nanoscale slip before the transition to gross slip as measured by moiré interferometry

The block position was measured seven times per second to ±5 nm accuracy by the optical pattern-matching method described above.

The results of a typical measurement are shown in Fig. 48.9b. At each large jump (denoted by diamonds), an equilibrium between tangential force and friction force exists, and following Amontons' law a coefficient of static friction can be determined according to

$$\mu_s = \frac{F_s}{F_n} , \tag{48.6}$$

where F_s (the static friction force opposing the spring force supplied by the linear suspension spring) and F_n (the electrostatic normal force) are the values associated with the static friction event. A more accurate coefficient of friction is found by taking the slope of the dashed line in Fig. 48.9b. In that case, adhesion is taken into account [48.54].

Taking advantage of the ±5 nm displacement resolution, in Fig. 48.9c the region just before a large jump can be expanded. Motion on the order of 100 nm is observed before the large jump. This nanometer-scale slip has been observed reproducibly over many measurements and is of concern for high-precision positioning applications. To understand this interesting characteristic in more detail, *Corwin* and *de Boer* have investigated the effect of three parameters:

- t_h – the time the nanotractor is held before the normal force ramp down begins
- F_h – the normal load at which the clamps are held before the ramp down
- $\dot{F}_n$ – the rate at which the normal force is ramped down [48.75].

Their effects are shown in Figs. 48.10–48.12 and described below.

In the data presented in Fig. 48.10a, the nanotractor is held at position $x = x_0$ and the normal load is held at F_h (designated by a vertical dashed line on the right) for hold time t_h. The normal load is then ramped down until an off-scale jump is observed. The experiment is repeated for a different hold time after the nanotractor is repositioned at $x = x_0$. The data for different hold times in Fig. 48.10a is offset by 0.1 μm in order to make it distinguishable. The circle for each hold time represents the onset of detectable slip. If the load is held for only a few seconds ($t_h \leq 32$ s) as it was in Fig. 48.9 ($t_h = 1$ s), frictional creep is observed before the transition to gross slip, as designated by the label "creep" in Fig. 48.10a. On the other hand, if it is held in place for a longer time ($t_h \geq 64$ s), the test structure reveals no motion before the transition to gross slip, as indicated by the label "off-scale jump" in the figure. There is also a critical normal force F_{nc}, as designated by a vertical dashed line. If detectable motion occurs before F_n reaches F_{nc}, the system exhibits frictional creep before the transition to gross slip. If F_n descends below F_{nc} before detectable slip, the transition to gross slip is abrupt. Hence, there is a bifurcation in the transition to motion – it either occurs as an inertial jump or as frictional creep. These measurements are highly reproducible (the same effects were observed over multiple fabrication lots and also if the hold time order was randomized) and show that the loading protocol matters in MEMS friction measurements. In Fig. 48.10b, the μ_s values, calculated from the circles in Fig. 48.10a, are plotted. A characteristic logarithmic aging coefficient β is found.

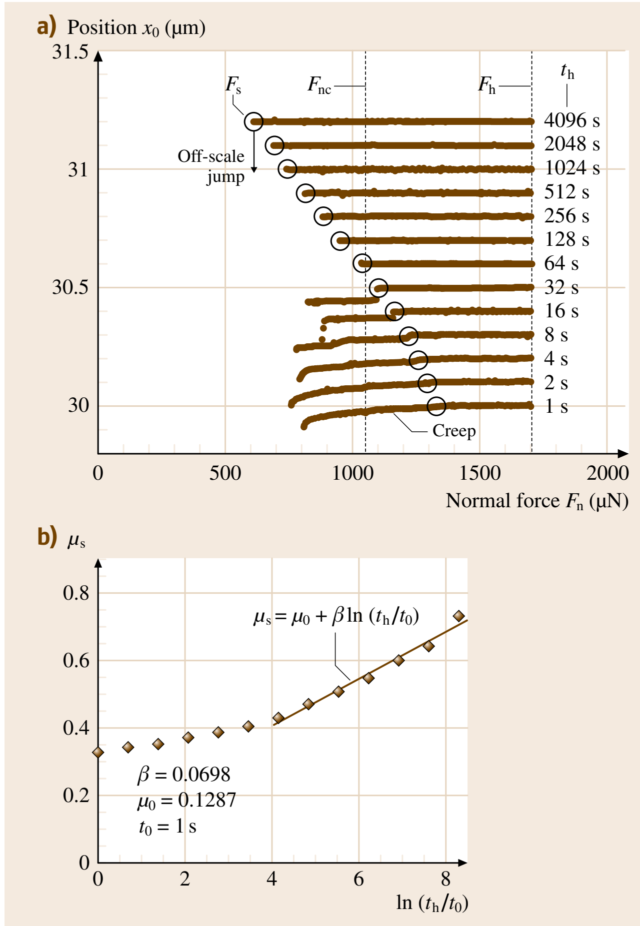

Fig. 48.10 **(a)** Complex aging behavior observed by varying the hold time t_h; see text for description. **(b)** The logarithmic aging behavior is characterized by the slope β ▶

In Fig. 48.11, the effect of changing the hold load F_h before the normal load ramp down is shown. Here it is seen that, as F_h is increased, the aging rate β decreases and approaches zero for sufficiently large F_h. Logarithmic frictional aging is a characteristic signature of rate–state behavior, and is generally attributed to material creep; that is, the contact area increases with time due to the heavy loading at the contacts [48.65], similar to in indentation creep. This has been directly observed in soda lime glass and acrylic plastic [48.76]. Hence, the result of Fig. 48.11 is counterintuitive. This effect can better be thought of as an increase in aging rate as the ratio of shear to normal force increases. A similar result has been reported for a rough glassy polymer on silanized glass [48.77] and can be ascribed to the associated biasing of a glassy material energy landscape [48.78, 79].

Although not shown, each F_h series in Fig. 48.11 is derived from a plot similar to Fig. 48.10a. From such plots a bifurcation in the transition to sliding is again observed, and F_{nc} remains the same, independent of F_h. A qualitative explanation for the existence of F_{nc} is as follows. If the interface ages significantly during the hold, then μ_s becomes large. As the normal load ramps down, F_n reaches a low value before motion initiates. Once this occurs, the contacts are rejuvenated, and μ_s becomes much lower. This large change in μ_s, coupled with the low value of F_n, results in an immediate transition to inertial sliding. Conversely, if t_h is small, the contacts do not age much. Therefore, F_n does not reach a very low value before the onset of motion. The small change in μ_s, coupled with the high value of F_n at which sliding initiates, results in only a very small change in position, and hence the slip on the surface is stable. Detailed measurements reported in [48.75] indeed show that this apparent frictional creep is a convolution of true frictional creep and the continuing normal force ramp down.

Although the dependence of μ_s on t_h in Figs. 48.10 and 48.11 demonstrates that there is an aging effect, the protocol for measuring this is not necessarily fully specified. The normal force ramp-down rate $\dot{F}_n$ may also affect the μ_s values because the state of the interface, in terms of the number of contacts per unit area, decreases while the normal load is ramped down. When the ramp-down time t_{rd} (on the order of tens of seconds for the data shown thus far) is on the order of t_h, an interaction

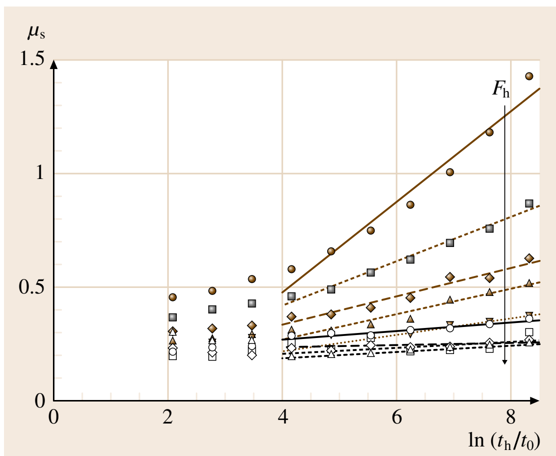

Fig. 48.11 Increasing the hold force F_h (from 1500 to 4800 μN here) decreases the aging rate

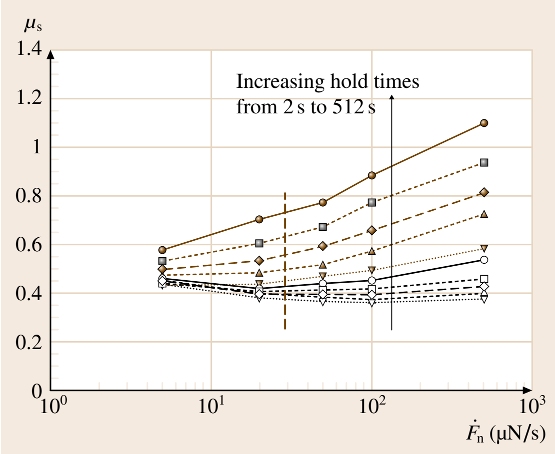

Fig. 48.12 By varying the ramp-down rate, μ_s changes by a factor of 3. In the previous plots (Figs. 48.10 and 48.11), the ramp-down rate was 20–35 μN/s, as indicated by the *dashed vertical line*

between t_{rd} and t_h is expected. When it is much greater than t_{rd}, t_h will possibly control the μ_s value.

The data presented in Fig. 48.12 show the strong effect of $\dot{F}_n$ on μ_s. Here, the ramp-down rate was increased by increasing the voltage increments during the ramp down, while the camera frame rate was fixed at seven frames per second. The ramp-down rate for Figs. 48.10 and 48.11 was 20–35 μN/s, while in Fig. 48.12 it is varied from 5 to 500 μN/s. Further increase of $\dot{F}_n$ was limited by the camera frame rate. For the largest $t_h = 512$ s, μ_s increases monotonically with $\dot{F}_n$. For the smallest t_h and $\dot{F}_n$ values, some aging occurs during the ramp down, which tends to increase the μ_s value for small $\dot{F}_n$. To obtain Fig. 48.12, a series of data similar to Fig. 48.10a was taken for each $\dot{F}_n$ value. Each value for μ_s in Fig. 48.12 was again taken from the first observable motion. Each plot revealed a bifurcation in the transition to slip, again with $F_{nc} \approx 1000$ μN.

48.2.3 Nanotractor Release Time Measurement

The data in Fig. 48.12 show that, even at the highest $\dot{F}_n$ value (where, the ramp-down time t_{rd} is much less than the hold time t_h), the μ_s value does not saturate. Given the strong dependencies observed, *Corwin* and *de Boer* considered the possibility that the concept of static friction may not be the most appropriate one for the normal force ramp-down test protocol [48.80]. Recently, the phenomenon of interface *deaging* has been directly measured on PMMA/PMMA interfaces [48.81]. There, history-dependent unloading and a true contact area that decreases with time in a deaging process whose time depends on prior aging were observed. The real contact area was directly observed using a high-speed camera with a total internal reflection method. Perhaps an important parameter characterizing the interface shear strength in these experiments is a release (or deaging) time.

In order to examine this idea, a series of experiments was carried out utilizing the maximum possible ramp-down rate (i. e., release on the order of 1 μs), and measurements of the release time were made. Details are provided in [48.80], and are briefly described here. The setup that was implemented is shown in Fig. 48.13. The nanotractor was walked to the initial position x_0 as shown in Fig. 48.13a. It was held at that position with a normal force F_h for a time t_h. Then, the load was *instantaneously* dropped to F_r. At this point, a high-speed camera (Phantom V 5.0) operating at 10 000 frames per second was triggered as shown in Fig. 48.13b, and frames were stored in the camera memory. Using simple dynamics calculations assuming $\mu_s = 0.3$ and a displacement resolution of 1 μm, the expected response time is 6 μs, significantly less than the time for one frame. If this calculation applies, the motion will always occur in the first frame.

Figure 48.14, however, shows that release times from less than 100 μs to almost 50 s are measured, spanning nearly six orders of magnitude. For fixed values of F_n and F_r, an increase in hold time t_h leads to an increase in release time t_r. Thus aging between

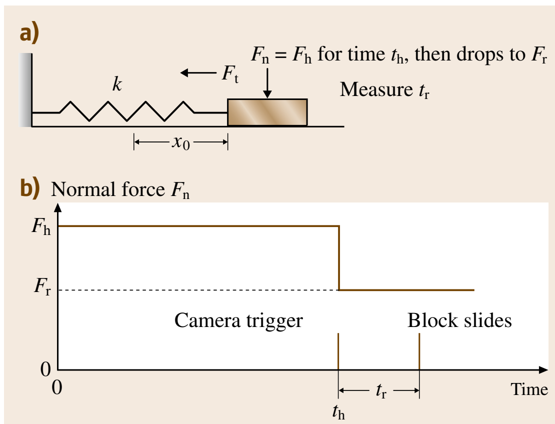

Fig. 48.13a,b Schematic of the release time test. **(a)** Nanotractor block against stretched spring, **(b)** timing diagram to measure release time t_r

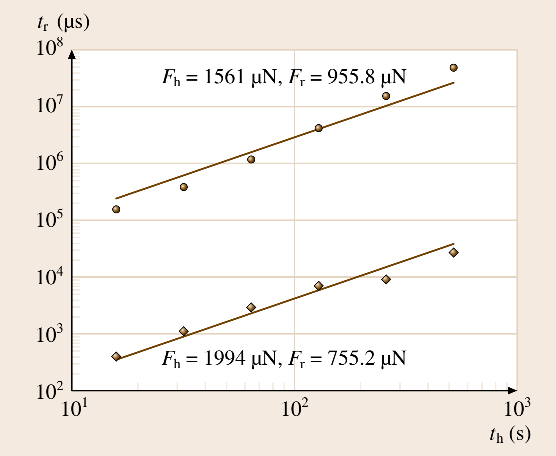

Fig. 48.14 Dependence of release time t_r on t_h

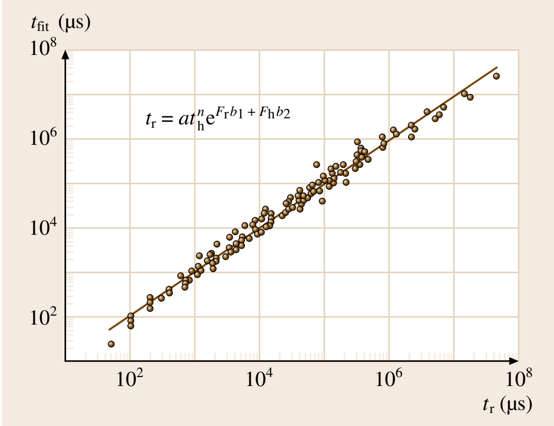

Fig. 48.15 Combining the fits from three different measurements, the data collapse onto a single fit ranging over six orders of magnitude of time

the two contacting surfaces is also evidenced in these measurements (assuming that deaging is directly related to aging [48.81]). The two data sets in Fig. 48.14 were taken for different pairs of the parameters F_h and F_r. The linear behavior suggests a power-law dependence of release time on hold time of the form $t_r \propto t_h^n$. The line through both sets of data are plotted with the same value of the exponent n, demonstrating that the scaling of t_r with t_h is independent of both F_h and F_r.

A direct demonstration that aging occurs was shown by resetting it after a hold. By moving the block by as little as 50 nm (a single step of the nanotractor) after aging but before dropping the release force, the release time enhancement due to aging was entirely removed.

Similar to Fig. 48.14, measurements of t_r as a function of F_r and F_h also revealed characteristic dependencies. A full functional form is a combination of the three dependencies, and can be written as

$$\log(t_r) = \log(a) + n\log(t_h) + b_1 F_r + b_2 F_h \,. \quad (48.7)$$

This data can be approximated by a least-squares fit with the four parameters, a, n, b_1, and b_2, extracted from Fig. 48.14 and the other measurements just mentioned. Figure 48.15 displays a plot of fitted release times t_{fit} versus measured release times and demonstrates that (48.7) fits the data well over six orders of magnitude of time.

These results show that release time in this system depends on the full load history through the hold time t_h, the hold force F_h, and also on the release force F_r. This memory effect is similar to observations by *Rubinstein* et al. [48.81]. Through measurements of the true contact area of PMMA blocks, they observed history-dependent unloading and a true contact area that decreased with time in a deaging process whose time depended on prior aging, similar to the measurement of release time. Viewing deaging time as a measure of prior aging, this empirical model can be thought of as revealing the functional dependencies of aging, and because unloading takes place almost instantaneously, this model does not depend on setting a particular ramp-down rate.

This observed deaging time behavior can qualitatively explain the previously observed dependencies of measured static friction coefficient on the ramp-down rate. If ramping down the normal force slowly, the contacting surfaces have more time to pull apart and measurable slip occurs at a higher normal force, leading to a smaller measured μ_s. When ramping down rapidly, the surfaces have less time to separate and measurable slip occurs at a much lower normal force, leading to a larger measured μ_s.

The aging effects reported above were observed on the FOTAS monolayer. It can be expected that the data will qualitatively change for different monolayers as well as different environmental conditions. Therefore, to fully assess the friction of a given monolayer for use in MEMS or nanoelectromechanical systems (NEMS) application, much more testing will be necessary.

Preliminary data indicates that, if a better ordered monolayer, e.g., OTS [48.82] is applied, results are substantially different. In particular, OTS is seen to exhibit significantly more creep. In the release time measurements, instead of observing a clearly identifiable release time after which motion ensued, an

OTS-coated nanotractor instead displayed continuous creep, moving at a much faster rate after the normal force was dropped. Similar behavior has been observed for the OTS-coated nanotractor in static friction measurements [48.55], where compared with the FOTAS-coated devices, OTS-coated devices showed much more creep. Also, measurements of μ_s and μ_d are nearly indistinguishable with OTS.

48.2.4 Stick–Slip Testing Using the Nanotractor

Stick–slip is a widely observed phenomenon, usually occurring at low spring constants and low velocities, as shown in Fig. 48.16a. At higher velocities or spring constants, steady sliding occurs. Very likely, the transition from stick–slip to steady sliding will be an important phenomenon to control and understand in microsystems. The friction test protocol used above is natural for microdevice testing schemes considering that the nanotractor is connected to the substrate via a spring, but is different from that of most friction measurements. More commonly in macroscale friction testing, normal load is held constant while tangential force is raised until slip is measured. Unlike conventional macroscale experiments, in the microscale measurements shown above, the apparent rate of aging β is not fundamental, but rather depends on the normal load ramp-down rate. To make more meaningful comparisons across the length scales, it is necessary to build a microfriction apparatus that is analogous to a conventional stick–slip apparatus.

A prototype system to measure stick–slip is shown in Fig. 48.16b. Here the nanotractor serves as a stepper motor providing a *constant-velocity* puller (stepper motors are also used as pullers in macroscale experiments; see, e.g., [48.62]). A folded-beam spring connects the nanotractor to a friction block. The spring separation is monitored using a vernier scale that extends *inside* the spring. The design of the friction block on the left of Fig. 48.16b is similar to that of a nanotractor clamp in which normal force is provided by electrostatic actuation. In this design, the spring constant is only changed by varying its line width, and hence the spring constant is fixed for a given structure. However, normal force can be easily varied on the same device.

A total travel distance of 300 μm is possible with this apparatus. Hence, a relatively large surface region can be sampled. Figure 48.16b schematically shows a device that has been moved 150 μm to the left in preparation for a test. To make measurements, a high-speed camera is again used. The nanotractor velocity is controlled by the step frequency and average velocities v up to 1 mm/s are possible.

Figure 48.17 shows that a stick–slip to steady sliding bifurcation can be induced by changing the spring constant. In Fig. 48.17a, $k = 0.2$ N/m and stick–slip is observed. In Fig. 48.17b $k = 2.0$ N/m and steady sliding

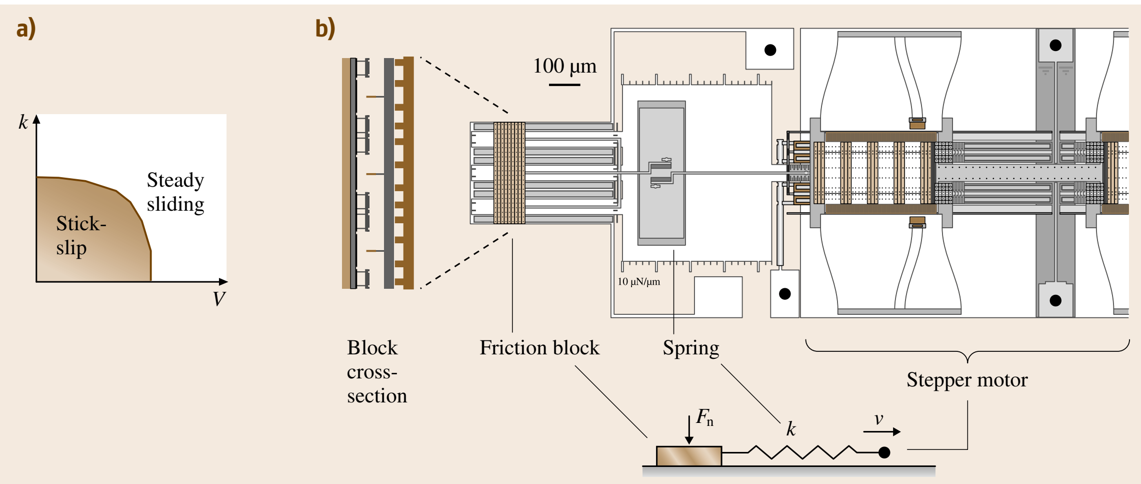

Fig. 48.16 **(a)** General form of kinetic phase diagram. **(b)** Surface-micromachined stick–slip pull system. The optical image shows a device that has been moved 150 μm to the left to maximize travel distance during the test. Here, the nanotractor becomes the puller. A folded beam with an internal vernier forms the spring of constant k and a structure similar to the nanotractor clamp becomes the friction block

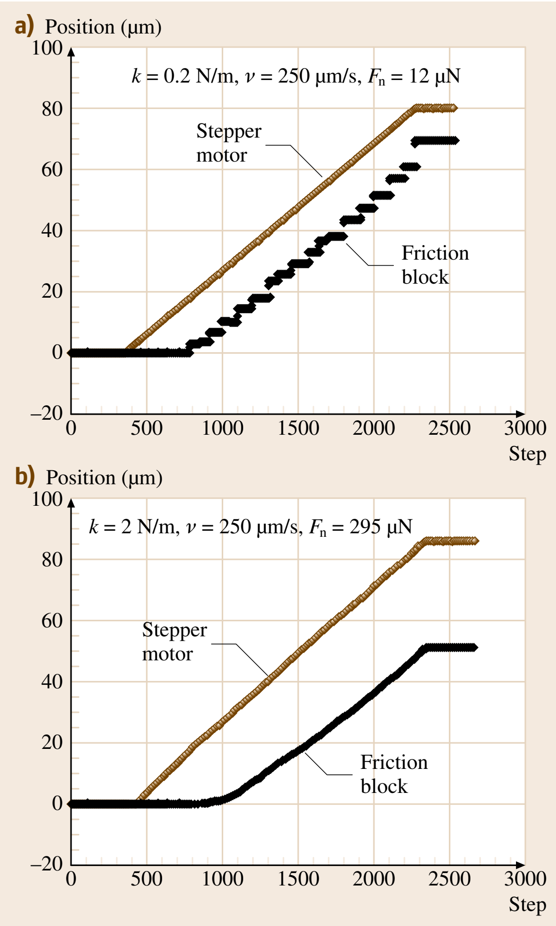

Fig. 48.17a,b Stick–slip results with an FOTAS coating. **(a)** $k = 0.2\,\mathrm{N/m}$, stick–slip; **(b)** $k = 2\,\mathrm{N/m}$, steady sliding

is observed. The same qualitative behavior occurred for each k, independent of velocity from 25 to $250\,\mu\mathrm{m/s}$. These preliminary experiments show that stick–slip exists and can be characterized with this apparatus. Much more work to understand these phenomena at this scale will be needed.

48.2.5 Wear Testing Using the Nanotractor

As a final example of friction phenomena that can be explored with the nanotractor, we discuss results of wear experiments. Normally in the walking process, the clamp voltage is changed from a large value (150 V) to zero before the clamp is moved. Here instead *Flater* et al. [48.56] reduced the clamp voltage to a nonzero value, typically 20 V. In these experiments, the nanotractor walked against a nonlinear load spring, developing a tangential force of $100\,\mu\mathrm{N}$ at each end of the travel. A nanotractor coated by a monolayer of FOTAS [48.72] consistently walked $27 \pm 2\,\mu\mathrm{m}$ for a fixed number of steps. Failure abruptly occurred at 7000 cycles. On the other hand, an oxide-coated nanotractor prepared by critical-point drying walked consistently over only 500 cycles. While it continued to operate, the distance traveled was highly sporadic, ranging from 0 to $25\,\mu\mathrm{m}$. Failure to walk occurred at 5000 cycles. Wear of the exposed polysilicon counterface at the end of the clamp can be imaged by AFM or SEM, as shown in [48.56].

These nanotractor measurements, including the dynamic friction measurement and the static friction measurements, required numerous experimental trials in order to gain the data. An assumption made is that the nanotractor friction does not change over the course of these measurements. The observation that the data is consistent from one experimental trial to the next supports this assumption. The observation that the FOTAS-coated nanotractor consistently walks for up to several thousand cycles even when loaded further supports these methods for taking data. Eventually, however, wear will affect these measurements, and this is an important issue being addressed by researchers [48.83, 84].

48.3 Concluding Remarks

These results on a nominally flat multiasperity polysilicon interface coated by a FOTAS monolayer show that Amontons' law (modified for the adhesion force due to van der Waals forces over the vast noncontacting areas) applies for dynamic friction, but not for static friction. This latter quantity rather depends strongly on loading protocol. We have described nanotribology measurements, microscale measurements, and various contact mechanics models. The *holy grail* in this field is to link these three areas using appropriate physical models. It is also important to apply data from friction measurements directly to actuator performance, and initial progress in this area has been reported [48.85]. Although the results presented here are mainly at the microscale, we imagine that similar test structures and actuator designs will also be of interest for NEMS. Surface roughness, controlled by grain growth and etching processes, may also be similar. Therefore, we expect that much of what is learned from microscale friction may apply to the nanoscale as well. Technologically, progress is continuing on many fronts. This includes the development of new materials such as SiC [48.86] and diamond-like materials [48.87], as well as methods to achieve improved hydrophobicity [48.88], and to reduce wear [48.83]. Taken together, significant technological impact can be expected from this burgeoning area of MEMS and NEMS interface science.

References

48.1 M.S. Rodgers, J.J. Sniegowski: Five-level polysilicon surface micromachine technology: application to complex mechanical systems, Solid-State Sens. Actuator Workshop, Hilton Head Island (1998) pp. 144–149

48.2 J.J. Sniegowski, M.P. de Boer: IC-compatible polysilicon surface micromachining, Annu. Rev. Mater. Sci. **30**, 299–333 (2000)

48.3 T. Akiyama, D. Collard, H. Fujita: Scratch drive actuator with mechanical links for self-assembly of three-dimensional MEMS, J. Microelectromech. Syst. **6**(1), 10–17 (1997)

48.4 E. Sarajlic: Electrostatic microactuators fabricated by vertical trench isolation technology. Ph.D. Thesis (University of Twente, Twente 2005)

48.5 L. Eldada: Advances in telecom and datacom optical components, Opt. Eng. **40**(7), 1165–1178 (2001)

48.6 E. Sarajlic, E. Berenschot, N. Tas, H. Fujita, G. Krijnen, M. Elwenspoek: High performance bidirectional electrostatic inchworm motor fabricated by trench isolation technology, TRANSDUCERS '05, 13th Int. Conf. Solid-State Sens. Actuators Microsyst. (2005) pp. 53–56

48.7 P. Vettiger, G. Cross, M. Despont, U. Drechsler, U. Dürig, B. Gotsmann, W. Häberle, M.A. Lantz, H.E. Rothuizen, R. Stutz, G.K. Binnig: The "Millipede" – nanotechnology entering data storage, IEEE Trans. Nanotechnol. **1**(1), 39–55 (2002)

48.8 J.M. Zara, S.M. Bobbio, S. Goodwin-Johansson, S.W. Smith: Intracardiac ultrasound scanner using a micromachine (MEMS) actuator, IEEE Trans. Ultrason. Ferroelectr. Freq. Control **47**(4), 984–993 (2000)

48.9 T. Akiyama, K. Shono: Controlled stepwise motion in polysilicon microstructures, J. Microelectromech. Syst. **2**(3), 106–110 (1993)

48.10 R.J. Linderman, V.M. Bright: Nanometer precision positioning robots utilizing optimized scratch drive actuators, Sens. Actuators A **91**, 292–300 (2001)

48.11 N. Tas, J. Wissink, L. Sander, T. Lammerink, M. Elwenspoek: Modeling, design and testing of the electrostatic shuffle motor, Sens. Actuators A **70**, 171–178 (1998)

48.12 M.P. de Boer, D.L. Luck, W.R. Ashurst, A.D. Corwin, J.A. Walraven, J.M. Redmond: High-performance surface-micromachined inchworm actuator, J. Microelectromech. Syst. **13**(1), 63–74 (2004)

48.13 E. Sarajlic, E. Berenschot, H. Fujita, G. Krijnen, M. Elwenspoek: Bidirectional electrostatic linear shuffle motor with two degrees of freedom, IEEE Int. Conf. MEMS (2005) pp. 391–394

48.14 G. Amontons: On the resistance originating in machines, Mém. Acad. R. A, 206–222 (1699), in French

48.15 F.P. Bowden, D. Tabor: *Friction and Lubrication of Solids: Part I* (Oxford Univ. Press, Oxford 1950)

48.16 H. Hertz: On the contact of elastic solids, J. Reine Angew. Math. **92**, 156–171 (1882), in German

48.17 K.L. Johnson, K. Kendall, A.D. Roberts: Surface energy and the contact of elastic solids, Proc. R. Soc. Lond. Ser. A **324**, 301–313 (1971)

48.18 B.V. Derjaguin, V.M. Muller, Y.P. Toporov: Effect of contact deformations on the adhesion of particles, J. Colloid Interface Sci. **53**(2), 314–326 (1975)

48.19 D. Tabor: Surface forces and surface interactions, J. Colloid Interface Sci. **58**, 2–13 (1977)

48.20 D. Maugis: Adhesion of spheres: The JKR-DMT transition using a Dugdale model, J. Colloid Interface Sci. **150**, 243–269 (1992)

48.21 J.F. Archard: Elastic deformation and the laws of friction, Proc. R. Soc. Lond. Ser. A **243**, 190–205 (1957)

48.22 R.W. Carpick, N. Agrait, D.F. Ogletree, M. Salmeron: Measurement of interfacial shear (friction) with an ultrahigh vacuum atomic force microscope, J. Vac. Sci. Technol. B **14**, 1289–1295 (1996)

48.23 M. Enachescu, R.J.A. van den Oetelaar, R.W. Carpick, D.F. Ogletree, C.F.J. Flipse, M. Salmeron: Observation of proportionality between friction and contact area at the nanometer scale, Tribol. Lett. **7**, 73–78 (1999)

48.24 M.A. Lantz, S.J. O'Shea, M.E. Welland, K.L. Johnson: Atomic force microscope study of contact area and friction on $NbSe_2$, Phys. Rev. B **55**, 10776–10785 (1997)

48.25 J.F. Archard: Contact and rubbing of flat surfaces, J. Appl. Phys. **24**, 981–988 (1953)

48.26 J.A. Greenwood, J.B.P. Williamson: Contact of nominally flat surfaces, Proc. R. Soc. Lond. Ser. A **295**, 300–319 (1966)
48.27 K.N.G. Fuller, D. Tabor: The effect of surface roughness on the adhesion of elastic solids, Proc. R. Soc. Lond. Ser. A **345**, 327–342 (1975)
48.28 D. Maugis: On the contact and adhesion of rough surfaces, J. Adhes. Sci. Technol. **10**(2), 161–175 (1996)
48.29 J.I. McCool: Comparison of models for the contact of rough surfaces, Wear **107**, 37–60 (1986)
48.30 B.N.J. Persson: On the nature of surface roughness with application to contact mechanics, sealing, rubber friction and adhesion, J. Phys. Condens. Matter **17**(44), 1071–1142 (2005)
48.31 N.R. Tas, C. Gui, M. Elwenspoek: Static friction in elastic adhesion contacts in MEMS, J. Adhes. Sci. Technol. **17**(4), 547–561 (2003)
48.32 W.R. Ashurst, M.P. de Boer, C. Carraro, R. Maboudian: An investigation of sidewall adhesion in MEMS, Appl. Surf. Sci. **212/213**, 735 (2003)
48.33 M.G. Lim, J.C. Chang, D.P. Schultz, R.T. Howe, R.M. White: Polysilicon microstructures to characterize static friction, Proc. IEEE MEMS Workshop, Napa Valley (1990) pp. 82–88
48.34 W.R. Ashurst, Y.J. Jang, L. Magagnin, C. Carraro, M.M. Sung, R. Maboudian: Nanometer-thin titania films with SAM-level stiction and superior wear resistance for reliable MEMS performance, Proc. 17th IEEE Int. Conf. MEMS (2004) pp. 153–156
48.35 W.R. Ashurst, C. Yau, C. Carraro, C. Lee, R.T. Howe, R. Maboudian: Alkene-based monolayer films as anti-stiction coatings for polysilicon MEMS, Sens. Actuators A **9**(3), 239–248 (2001)
48.36 D.C. Senft, M.T. Dugger: Friction and wear in surface-micromachined tribological test devices, Proc. SPIE **3224**, 31–38 (1997)
48.37 W.M. van Spengen, J.W.M. Frenken: The Leiden tribometer: Real time dynamic friction loop measurements with an on-chip tribometer, Tribol. Lett. **28**, 149–156 (2007)
48.38 S.J. Timpe, K. Komvopoulos: The effect of adhesion on the static friction properties of sidewall contact interfaces of microelectromechanical devices, J. Microelectromech. Syst. **15**(6), 1612–1621 (2006)
48.39 S.J. Timpe, K. Komvopoulos: Microdevice for measuring friction and adhesion properties of sidewall contact interfaces of microelectromechanical systems, Rev. Sci. Instrum. **78**, 065106-1–065106-9 (2007)
48.40 R.W. Carpick, D.F. Ogletree, M. Salmeron: A general equation for fitting contact area and friction versus load measurements, J. Colloid Interface Sci. **211**(2), 395–400 (1997)
48.41 G.J. Leggett: Friction force microscopy of self-assembled monolayers: Probing molecular organisation at the nanometre scale, Anal. Chim. Acta **479**, 17–38 (2003)
48.42 Y.L. Chen, J.N. Israelachvili: Effects of ambient conditions on adsorbed surfactant and polymer monolayers, J. Phys. Chem. **96**, 7752–7760 (1992)
48.43 J.B.D. Green, M.T. McDermott, M.D. Porter, L.M. Siperko: Nanometer-scale mapping of chemically distinct domains at well-defined organic interfaces using frictional force microscopy, J. Phys. Chem. B **99**(27), 10960–10965 (1995)
48.44 G.Y. Liu, P. Fenter, C.E.D. Chidsey, D.F. Ogletree, P. Eisenberger, M. Salmeron: An unexpected packing of fluorinated n-alkane thiols on Au(111): A combined atomic-force microscopy and x-ray diffraction study, J. Chem. Phys. **101**(5), 4301–4306 (1994)
48.45 M.T. McDermott, J.B.D. Green, M.D. Porter: Scanning force microscopic exploration of the lubrication capabilities of n-alkanethiolate monolayers chemisorbed at gold: Structural basis of microscopic friction and wear, Langmuir **13**, 2504–2510 (1997)
48.46 E.W. van der Vegte, G. Hadziioannou: Scanning force microscopy with chemical specificity: An extensive study of chemically specific tip-surface interactions and the chemical imaging of surface functional groups, Langmuir **13**(16), 4357–4368 (1997)
48.47 Y. Liu, D.F. Evans, Q. Song, D.W. Grainger: Structure and frictional properties of self-assembled surfactant monolayers, Langmuir **12**(5), 1235–1244 (1996)
48.48 B.D. Beake, G.J. Leggett: Friction and adhesion of mixed self-assembled monolayers studied by chemical force microscopy, Phys. Chem. Chem. Phys. **1**, 3345–3350 (1999)
48.49 H.I. Kim, T. Koini, T.R. Koini, S.S. Perry: Systematic studies of the frictional properties of fluorinated monolayers with atomic force microscopy: Comparison of CF_3- and CH_3-terminated films, Langmuir **13**(26), 7192–7196 (1997)
48.50 E.W. van der Vegte, A. Subbotin, G. Hadziioannou, P.R. Ashton, J.A. Preece: Nanotribological properties of unsymmetrical n-dialkyl sulfide monolayers on gold: Effect of chain length on adhesion, friction, and imaging, Langmuir **16**, 3249–3256 (2000)
48.51 E.D. Reedy: Thin-coating contact mechanics with adhesion, J. Mater. Res. **21**(10), 2660–2668 (2006)
48.52 E.D. Reedy: Contact mechanics for coated spheres that includes the transition from weak to strong adhesion, J. Mater. Res. **22**(9), 2617–2622 (2007)
48.53 W.R. Ashurst, C. Yau, C. Carraro, R. Maboudian, M.T. Dugger: Dichlorodimethylsilane as an anti-stiction monolayer for MEMS: A comparison to the octadecyltrichlosilane self-assembled monolayer, J. Microelectromech. Syst. **10**(1), 41–49 (2001)
48.54 A.D. Corwin, M.P. de Boer: Effect of adhesion on dynamic and static friction in surface micromachining, Appl. Phys. Lett. **84**(13), 2451–2453 (2004)

48.55 A.D. Corwin, M.D. Street, R.W. Carpick, W.R. Ashurst, M.P. de Boer: Pre-sliding tangential deflections can govern the friction of MEMS devices, 2004 ASME/STLE Jt. Int. Tribol. Conf., Long Beach (2004) pp. TRIB2004-64630
48.56 E.E. Flater, A.D. Corwin, M.P. de Boer, M.J. Shaw, R.W. Carpick: In-situ wear studies of surface micromachined interfaces subject to controlled loading, Wear **260**(6), 580–593 (2006)
48.57 C. Carraro, O.W. Yauw, M.M. Sung, R. Maboudian: Observation of three growth mechanisms in self-assembled monolayers, J. Phys. Chem. B **102**(23), 4441–4445 (1998)
48.58 E.E. Flater, W.R. Ashurst, R.W. Carpick: Nanotribology of octadecyltrichlorosilane monolayers and silicon: Self-mated versus unmated interfaces and local packing density effects, Langmuir **23**(18), 9242–9252 (2007)
48.59 B.G. Bush, F.W. DelRio, J. Opatkiewiez, R. Maboudian, C. Carraro: Effect of formation temperature and roughness on surface potential of octadecyltrichlorosilane self-assembled monolayer on silicon surfaces, J. Phys. Chem. A **111**, 12339–12343 (2007)
48.60 J.H. Dieterich: Time-dependent friction in rocks, J. Geophys. Res. **77**(20), 3690–3697 (1972)
48.61 J.H. Dieterich, B. Kilgore: Implications of fault constitutive properties for earthquake prediction, Proc. Natl. Acad. Sci. USA **93**, 3787 (1996)
48.62 F. Heslot, T. Baumberger, B. Perrin, B. Caroli, C. Caroli: Creep, stick-slip and dry-friction dynamics: experiments and a heuristic model, Phys. Rev. E **49**(6), 4973–4988 (1994)
48.63 J.R. Rice, A.L. Ruina: Stability of frictional slipping, J. Appl. Mech. **50**(2), 343–349 (1983)
48.64 A.L. Ruina: Slip instability and state variable friction laws, J. Geophys. Res. **88**(NB12), 359–370 (1983)
48.65 P. Berthoud, T. Baumberger, C. G'Sell, J.-M. Hiver: Physical analysis of the state- and rate-dependent friction law: static friction, Phys. Rev. B **59**(22), 14313–14327 (1999)
48.66 T. Baumberger, C. Caroli, B. Perrin, O. Ronsin: Nonlinear analysis of the stick-slip bifurcation in the creep-controlled regime of dry friction, Phys. Rev. E **51**(5), 4005–4010 (1995)
48.67 Y.F. Lim, K. Chen: Dynamics of dry friction: A numerical investigation, Phys. Rev. E **58**(5), 5637–5642 (1998)
48.68 W.R. Chang, I. Etsion, D.B. Bogy: An elastic-plastic model for the contact of rough surfaces, J. Tribol. Trans. ASME **109**, 257–263 (1987)
48.69 Y. Ning, A.A. Polycarpou: Extracting summit roughness parameters from random Gaussian surfaces accounting for asymmetry of the summit heights, J. Tribol. Trans. ASME **126**(4), 761–766 (2004)
48.70 F.W. DelRio, M.P. de Boer, J.A. Knapp, E.D. Reedy, P.J. Clews, M.L. Dunn: The role of van der Waals forces in adhesion of micromachined surfaces, Nat. Mater. **4**(8), 629–634 (2005)
48.71 D.J. Dickrell, M.T. Dugger, M.A. Hamilton, W.G. Sawyer: Direct contact-area computation for MEMS using real topographic surface data, J. Microelectromech. Syst. **16**(5), 1263–1268 (2007)
48.72 M.G. Hankins, P.J. Resnick, P.J. Clews, T.M. Mayer, D.R. Wheeler, D.M. Tanner, R.A. Plass: Vapor deposition of amino-functionalized self-assembled monolayers on MEMS, Proc. SPIE **4980**, 238–247 (2003)
48.73 Y.H. Cho, A.P. Pisano, R.T. Howe: Viscous damping model for laterally oscillating microstructures, J. Microelectromech. Syst. **3**(2), 81–87 (1994)
48.74 A.D. Corwin, M.P. de Boer: Frictional aging and sliding bifurcation in monolayer-coated micromachines, J. Microelectromech. Syst. **18**(2), 250–262 (2009)
48.75 A.D. Corwin, M.P. de Boer: A linearized method to measure dynamic friction of microdevices, Exp. Mech. **49**(3), 395–401 (2009)
48.76 J.H. Dieterich, B.D. Kilgore: Direct observations of frictional contacts – New insights for state-dependent properties, Pure Appl. Geophys. **143**(1–3), 283–302 (1994)
48.77 L. Bureau, T. Baumberger, C. Caroli: Rheological aging and rejuvenation in solid friction contacts, Eur. Phys. J. E **8**(3), 331–337 (2002)
48.78 J. Rottler, M.O. Robbins: Unified description of aging and rate effects in yield of glassy solids, Phys. Rev. Lett. **95**(22), 225504–1–225504–4 (2005)
48.79 P. Sollich: Rheological constitutive equation for a model of soft glassy materials, Phys. Rev. E **58**(1), 738–759 (1998)
48.80 A.D. Corwin, M.P. de Boer: Frictional deaging in micromachined surfaces, J. Appl. Phys. (2009), submitted
48.81 S.M. Rubinstein, G. Cohen, J. Fineberg: Contact area measurements reveal loading-history dependence of static friction, Phys. Rev. Lett. **96**, 256103 (2006)
48.82 U. Srinivasan, M.R. Houston, R.T. Howe, R. Maboudian: Alkyltrichlorosilane-based self-assembled monolayer films for stiction reduction in silicon micromachines, J. Microelectromech. Syst. **7**(2), 252–260 (1998)
48.83 D.B. Asay, M.T. Dugger, J.A. Ohlhausen, S.H. Kim: Macro- to nanoscale wear prevention via molecular adsorption, Langmuir **24**(1), 155–159 (2008)
48.84 S.S. Mani, J.G. Fleming, J.J. Sniegowski, M.P. de Boer, L.W. Irwin, J.A. Walraven, D.M. Tanner, D.A. LaVan: Selective W for coating and releasing MEMS devices, Mater. Res. Soc. Symp. Proc. **605**, 135–140 (2000)
48.85 M. Patrascu, S. Stramigioli: Stick-slip actuation of electrostatic stepper micropositioners for data storage – The microWalker, Proc. 2005 Int. Conf. MEMS NANO Smart Syst. (2005) pp. 81–86

48.86 M. Mehregany, C.A. Zorman: SiC MEMS: Opportunities and challenges for applications in harsh environments, Thin Solid Films **356**, 518–524 (1999)
48.87 S. Cho, I. Chasiotis, T.A. Friedmann, J.P. Sullivan: Young's modulus, Poisson's ratio and failure properties of tetrahedral amorphous diamond-like carbon for MEMS devices, J. Micromech. Microeng. **15**(4), 728–735 (2005)
48.88 B. Bhushan, M. Nosonovsky, Y.C. Jung: Towards optimization of patterned superhydrophobic surfaces, J. R. Soc. Lond. Interface **4**(15), 643–648 (2007)